Characterising horizontal two-phase flows using Structured-Planar Laser-Induced Fluorescence (S-PLIF) coupled with Simultaneous Two-Phase PIV (S2P-PIV)

A. Abou Sherif*, D. B. Hann, K. Johnson

Faculty of Engineering, University of Nottingham, UK
*Corresponding author: ahmed.abousherif@nottingham.ac.uk

Keywords: structured-planar laser-induced fluorescence, simultaneous two-phase particles image velocimetry, two-phase, disturbance regime.

ABSTRACT

Understanding the physics that underpins the behaviours of two-phase flows is immensely useful for a diverse number of industries, including oil and gas, nuclear and aerospace. Stratified air-liquid two-phase flows are amenable to the application of two-phase PIV but this is often only possible if PIV processing parameters can be chosen to match the separate gas and liquid phase image sets. Accurate interface location detection is therefore extremely important to facilitate appropriate masking during analysis. This paper examines the effectiveness of using the Structured-Planar Laser-Induced Fluorescence (S-PLIF) method to aid in the accurate capture and processing of simultaneous two-phase PIV (S2P-PIV) for a gas-sheared liquid flow. Prior S2P-PIV work made use of direct interface detection, using contrast on images from the air-side camera. However, this method proved limiting in higher gas-shear cases, when the highly wavy nature of the flow prevented the camera from seeing all of the interface. An alternative prior approach using the liquid-side camera and the planar laser-induced fluorescence (PLIF) technique often led to large errors due to reflections from the free surface. Interface detection using the S-PLIF method facilitates a clearer delineation between the two phases, through analysis of the change in structure of the incident light, significantly reducing errors generated by the traditional PLIF. This then facilitates higher quality PIV analysis, both because interface identification is far more accurate and also because frame specific masking, of the individual phases, can be more automated. This paper presents air/water data from a rectangular channel with a liquid flowrate of 8 litres per minute and superficial gas velocities in the range 1 - 14 ms^{-1}. Data capture of the two phases is concurrent with the developed S-PLIF approach used to locate the interface, enabling separate and more accurate PIV analysis of the two phases over a wider parametric range than was previously possible. The data analysis shows that the transition to the disturbance/roll wave regimes is associated with a change in the liquid's axial velocity profile and a significant increase in normalised axial velocity root-mean-square velocity fluctuation. Data-sets from this work can be used to accurately describe high-speed gas sheared two-phase flows that will be extremely useful for CFD model development and validation.

1. Introduction

Understanding the physics that underpins the behaviours of two-phase flows is immensely useful for a diverse number of industries, including oil and gas, nuclear and aerospace. Multiphase flow

has therefore been a popular topic of research for decades. The academic and industrial dedication to the field has brought with it a multitude of developments in the techniques used to measure and validate the relevant fundamental physics. The advancements made in optical capture methods have created a dependable platform for the sector, leading to the generation of more accurate and precise data-sets. These can be used in the development of more robust and reliable CFD models, ultimately facilitating the creation of more environmentally friendly and cost-effective design solutions.

The work presented in this document introduces part of an ongoing research project in which Structured-Planar Laser-Induced Fluorescence (S-PLIF), coupled with Simultaneous Two-Phase PIV (S2P-PIV), is used to characterise the behaviour of two-phase gas-sheared liquid flows in a horizontally orientated rectangular cross-section channel. One of the key, overarching, objectives of the project is to expand on existing data and understanding of two-phase flow in horizontal rectangular channels, building on prior work including Fabre et al. (1987), who used LDA and capacitance probes, Cherdantsev et al. (2014), who used LIF and Cherdantsev et al. (2019), who applied a combination of brightness-based LIF and PLIF. This specific publication focuses on documenting the developments centred around the experimental techniques used for the data capture and analysis, in particular, using S-PLIF to aid in the correct processing of two-phase PIV work.

The S-PLIF method was developed by researchers at Imperial College London with successive developments documented in Charogiannis et al. (2018), Charogiannis & Markides (2019) and Charogiannis et al. (2019). S-PLIF was developed largely in parallel with research validating planar laser-induced fluorescence (PLIF) data using the brightness-based laser-induced fluorescence (BBLIF) technique as documented in Cherdantsev et al. (2018), with further development in Cherdantsev et al. (2019).

In Cherdantsev et al. (2018) and Cherdantsev et al. (2019), a single, non-structured, laser sheet was used to excite fluorescent dye in the liquid film of an annular air-water two-phase flow inside a vertically orientated Fluorinated Ethylene Propylene pipe (material chosen to match the refractive index of water). The researchers used two cameras to capture the results of each technique simultaneously, to allow for a direct temporal comparison. Their experiments investigated the flow in various states and some of the findings showed that when the gas-liquid interface was smooth, the PLIF method overestimated the film thickness as a result of the reflection of the excited light on the free surface. They also found that over estimation increased with decreasing angle between the axis of the laser sheet and the camera. While it was found that areas of the images that captured local features recorded as light intensity maxima or minima were better estimated by the PLIF capture, areas of the capture where there were steep slopes or where the film was agitated caused over estimation of film thickness when using the BBLIF method.

In 2019, Charogiannis et al. (2019) published work that described a novel adaption of the PLIF method, namely the structured-PLIF method, which uses a structured light sheet instead of an

unstructured one. It was found that the columns of light that were formed could be used to reduce/eliminate the errors in PLIF-derived film thickness measurements. The regular spatial modulation of laser light created alternating bright and dark regions where, at the true surface, the bright columns would change direction or distort (depending on the regime of the flow), allowing for the gas-liquid interface coordinates to be more accurately estimated. This ultimately helped to eliminate the error created by reflections at the free surface. In their work, Charogiannis et al. also experimented with the capture of simultaneous S-PLIF and PIV measurements in the liquid phase.

The research presented in this paper takes the methodology presented in Charogiannis et al. (2019) a step further by using the S-PLIF method to aid in the capture and processing of simultaneous two-phase PIV (S2P-PIV). However, in contrast to the original annular flow work, the presented research looks at gas-sheared liquid two-phase flow in a horizontally orientated rectangular cross-section duct. For most of the cases, the flow was stratified with the bulk of the liquid phase travelling along the lower section of the channel and the gas phase travelling along the upper section of the channel. This allows for capture of the two phases separately, but simultaneously.

Figure 1 shows example images which highlight signature features of the target flows that this research aims to characterise.

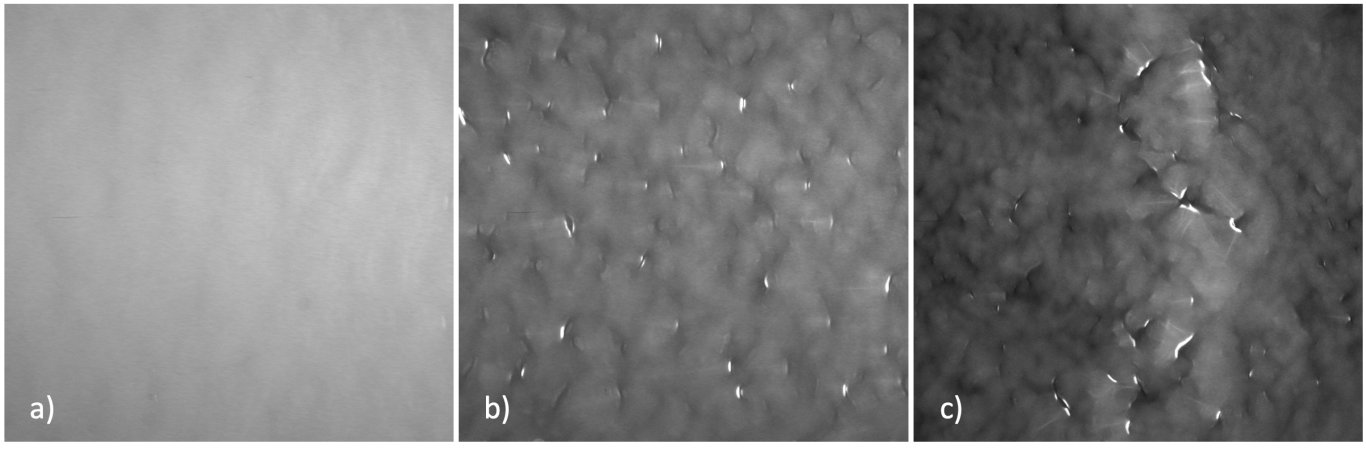

Figure 1. Sample frames from BBLIF image data (Abou Sherif et al. (2023)): (a) 2D regime (b) 3D regime (c) disturbance regime

These images were taken on the rig described in Section 2, using the BBLIF method in a separate experimental campaign Abou Sherif et al. (2023). The images were captured from below with the camera sensor parallel to the channel base, therefore only the liquid phase is visible. The brighter parts of each image denote increased liquid thickness and the darker parts signify decreased liquid thickness. Fig. 1a shows the surface condition in the 2D regime flow state, where the waves observed are small in amplitude, have large wavelengths and extend the entire span of the channel. Therefore the resultant brightness across the image is relatively uniform. Fig. 1b shows the surface condition in the 3D regime flow state, where small amplitude ripple waves are scattered across

the surface. These are denoted by the dimmer parts of the image (wave troughs) and the brighter parts (wave peaks). Finally, Fig 1c shows the disturbance wave regime state, where sweeping roll waves travel along a base film of 3D ripple waves all moving in the streamwise direction. The roll waves move at a higher relative speed to the base film. The presence of roll waves is made evident by the passing, brighter, feature that can be seen in the centre of the example frame of Fig. 1c.

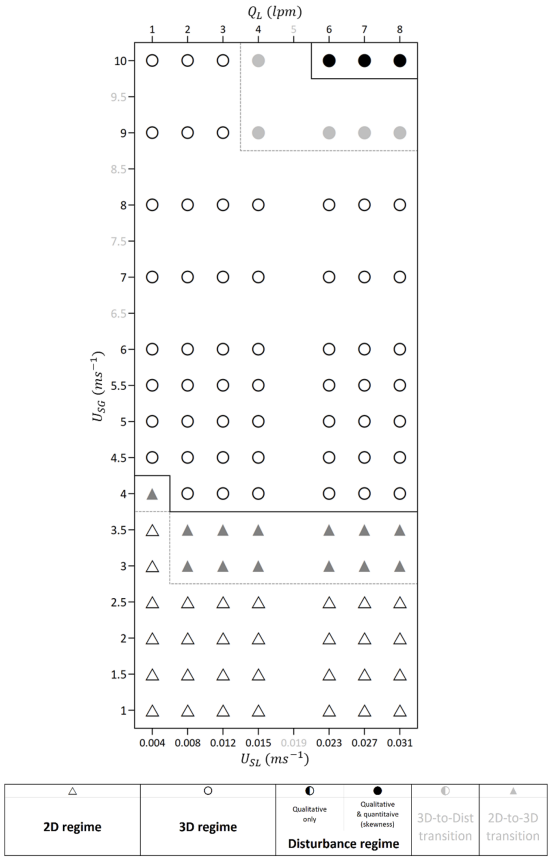

Figure 2. BBLIF water only two-phase flow pattern map

Figure 2 shows a flow regime map from BBLIF work on this rig, presented at the 11th International Conference on Multiphase Flow (Abou Sherif et al. (2023)). The regime transition regions defined on this flow pattern map were characterised by tracking the change in mean film thickness regression trends and data skewness. From this we can see that the transition from 2D to 3D regime occurred, for most of the liquid flow rate cases, at $U_{SG} = 4\ ms^{-1}$. And transition into the disturbance regime occurred at $U_{SG} = 10\ ms^{-1}$ between $U_{SL} = 0.015\ ms^{-1}$ and $U_{SL} = 0.031\ ms^{-1}$. We are particularly interested in the 8 LPM case for the present research.

This regime map introduces some of the topics discussed in this paper, where trends in the first and second order statistics, of the velocity vector maps, will be used to aid in characterising transition into the disturbance regime, corroborating that of the BBLIF data presented on Fig 2.

2. Experimental test facility

2.1. Two-phase flow rig

Experimental work on versions of the test facility illustrated in Figure 3 has been conducted, in abundance, in the past and the rig and experimental outcomes are documented in the literature. Particularly relevant are Hann et al. (2018) who investigated bubble entrapment, Sinha et al. (2021) who extended the bubble entrapment work through varying liquid properties and more recently, Cherdantsev (2023), who investigated disturbance waves. In this current research the main rig and methodology developments are concerned with the acquisition setup and the use of S-PLIF aided S2P-PIV.

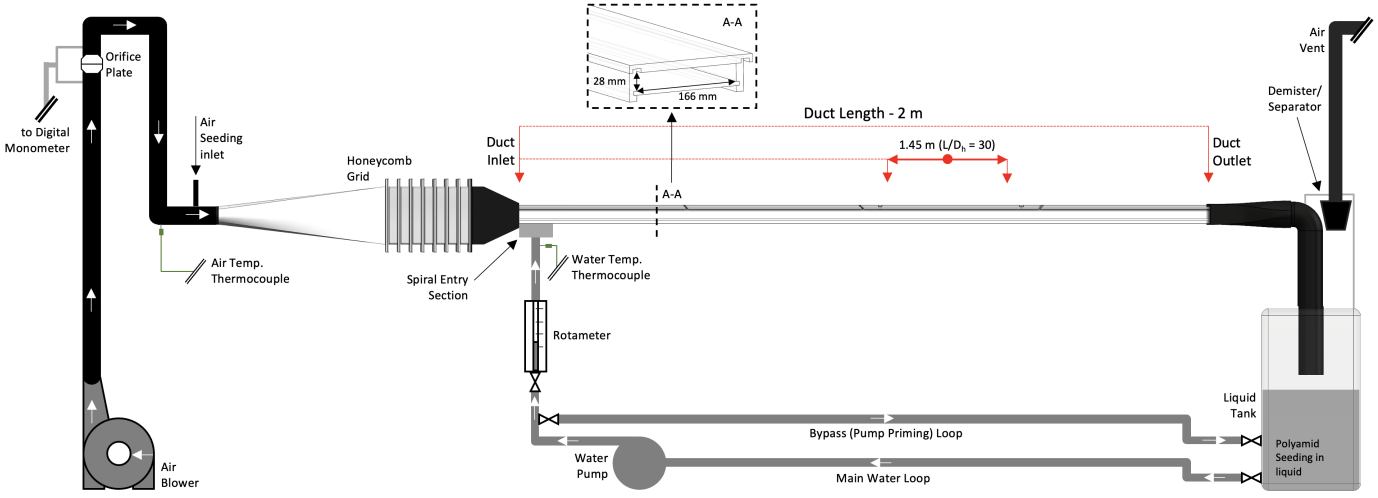

Figure 3. Experimental test rig

The main rig is centred around a 2-meter-long channel with width and height cross-sectional dimensions of $0.166\ m$ x $0.028\ m$. The liquid phase was introduced using a centrifugal pump and entered the channel through a spiral entry plate into the lower half of the channel (a closed loop system was used to recirculate the the liquid flow). The liquid flow rate was measured and monitored using a calibrated rotameter. A constant velocity air blower was used to introduce external ambient air, passing it through a honeycomb grid, to flatten the flow profile, before it entered the upper section of the channel. The air flow was monitored using an orifice plate, calibrated to velocity measurements taken at the test/acquisition section during work conducted prior to this. The acquisition section was located $1.45\ m$ ($L/D_h = 30$) downstream of the duct inlet.

2.2. Optical acquisition apparatus setup

Figure 4 shows the configuration of the acquisition equipment used in the capture of the S-PLIF coupled with S2P-PIV while Figure 5 shows a photograph of the rig and equipment in operation. Two Phantom v12.1 high-speed cameras were used to capture 12-bit images, each with an image size of 1280 x 800 $pixels$. The cameras were synchronised with a $15\ mJ$ Litron laser ($527\ nm$ wavelength) in a way that created a setup for double laser pulse and corresponding camera exposure. The air-side (upper) camera was tilted down at 2° and captured the light that scattered off the air seeding particles illumined directly by the laser, through the channel side wall. A Dantec Dynamics seeding generator was used to introduce a water-Glycerol (Glycerol 7% concentration) mist into the air stream, with a mean particle diameter of $3\ \mu m$. This air seeding was fed into the flow upstream of the honeycomb grid, with seeding flow rate monitored using an inline calibrated mass flow meter.

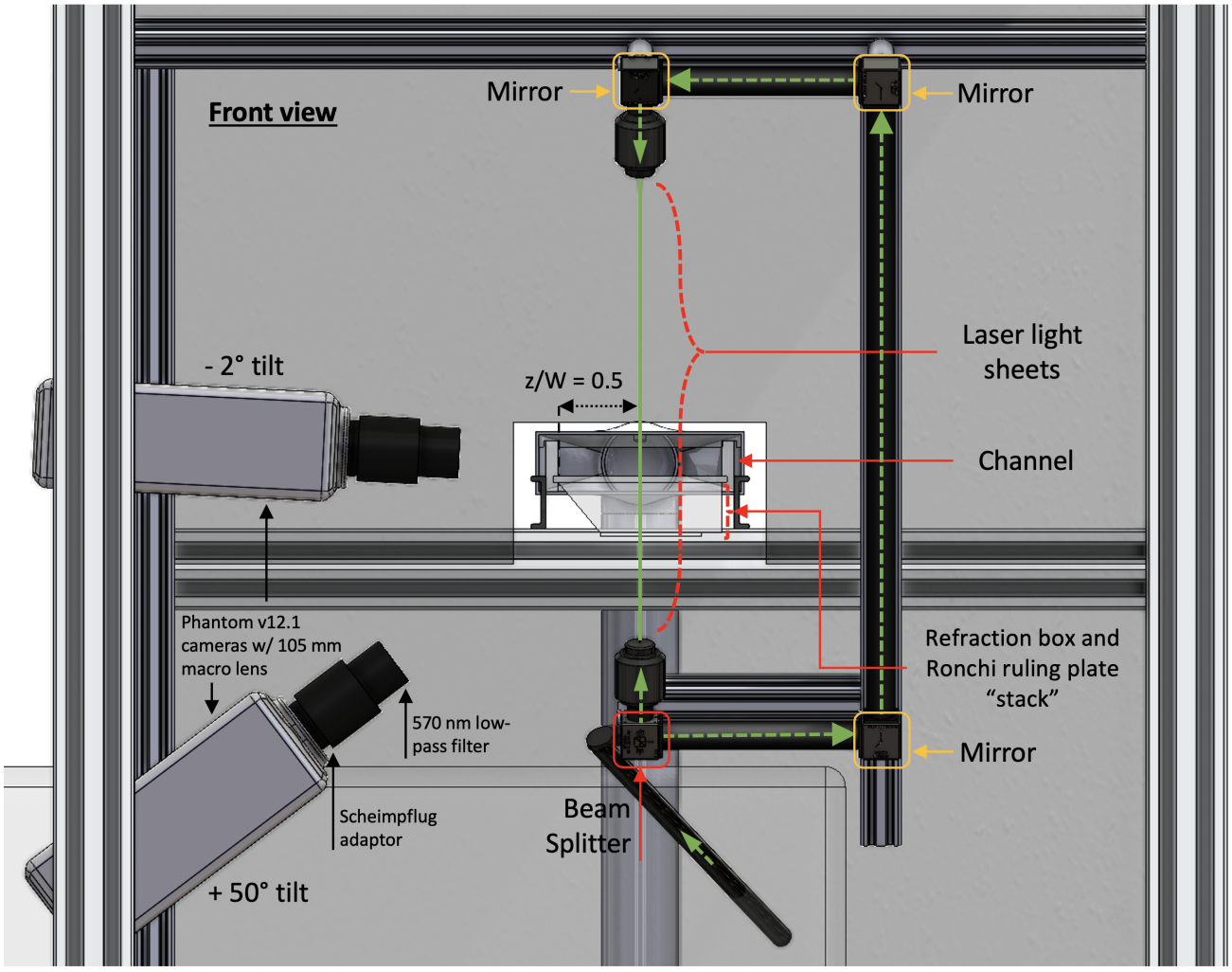

Figure 4. S-PLIF coupled S2P-PIV instrumentation setup

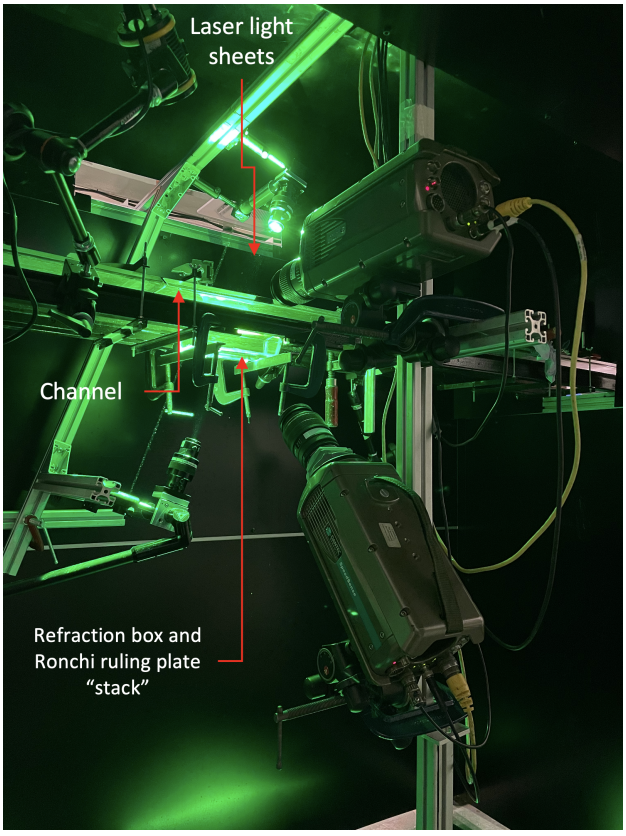

Figure 5. S-PLIF coupled S2P-PIV instrumentation in operation

The liquid-phase (lower) camera was tilted up at 50° and captured the light emitted from the laser excited dye in the liquid phase, as well as the light emitted from the dyed polyamid seeding particles (mean diameter: $20\mu m$) suspended in the liquid phase. Both the particles and liquid phase used the same dye; Rhodamine 6G. The liquid phase had a dye concentration of only $1\ mg/l$ so as to not overpower the visibility of the particles. A 570 nm long-pass filter was used on the liquid-side camera lens so that there was only capture of the laser-excited light and none of the laser's native 527 nm wavelength light.

A Ronchi ruling plate, with $1\ mm$ line spacing, was mounted directly to the bottom of the refraction correction box (used to compensate for the steep capture angle). The Ronchi ruling plate structured the incident light from the lower/liquid-side light sheet optic, which was angled at 30° to the streamwise normal, as this helped promote a clearer delineation between the phases. The air-side light sheet optic illuminated the air-seeding with a solid light sheet. Sample images of the raw and processed masked recordings can be seen in Figures 6 and 8.

3. Data Processing

3.1. S-PLIF image processing

Figure 6 shows a pre-processing flowchart and sample output illustrations, for each regime, of the S-PLIF derived true film height detection. Images from the liquid phase camera (illuminated by the structured light) were those used for the S-PLIF part of the work.

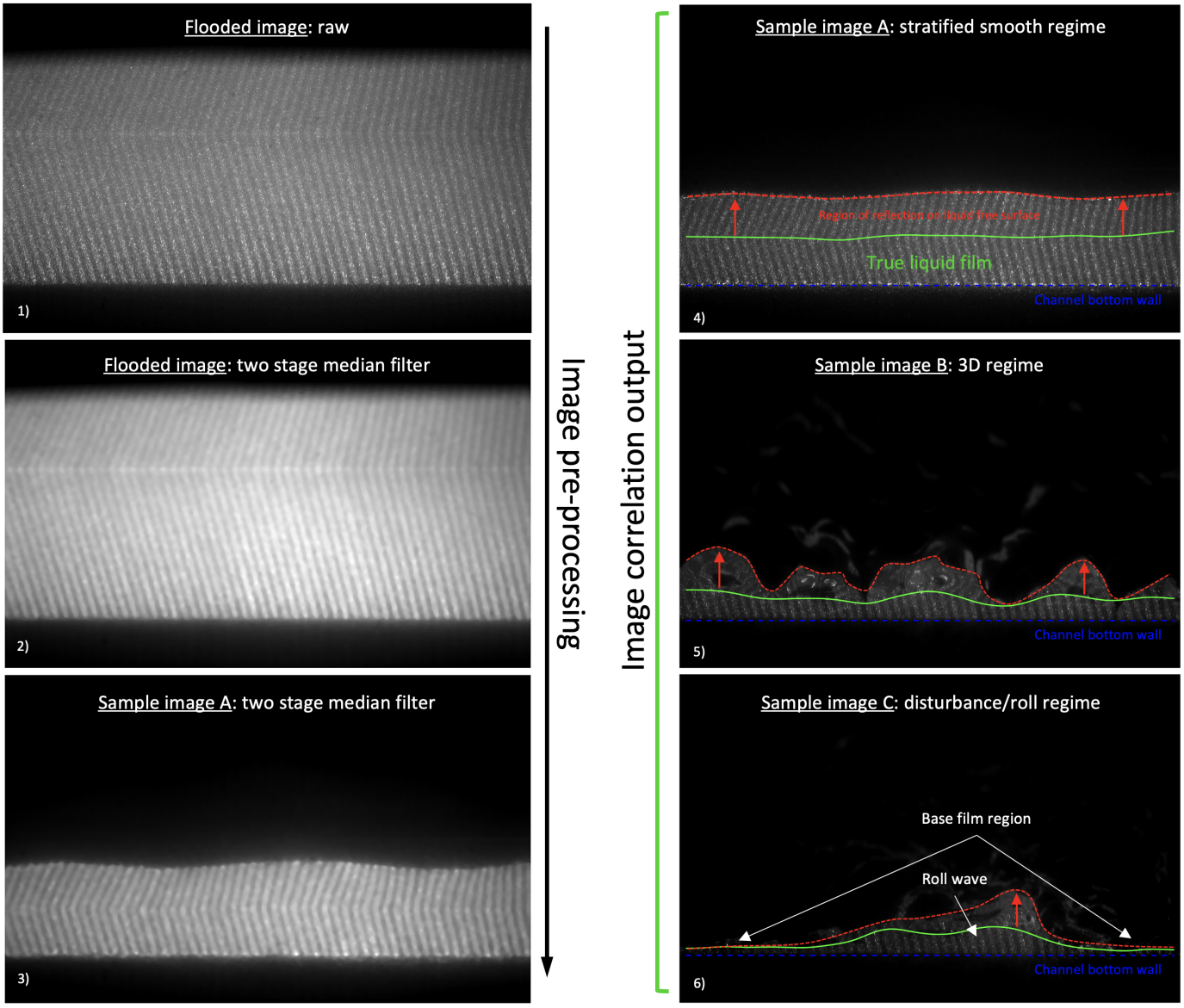

Figure 6. S-PLIF image pre-processing order (left flow chart) and interface detection sample images from each regime (right column)

Images (1) and (2) of Figure 6, show the raw and median filtered images, respectively, of the

flooded channel image. Image (3) of Figure 6 shows the median filtered image of a stratified smooth sample case (unprocessed version seen in the underlay of image (4)). The flooded channel section was generated by forming temporary upstream and downstream dams in the channel, opposite of the acquisition section. As shown in Figure 7 the volume created by the dams was then filled to the top of the channel with a sample from the liquid in the liquid loop tank. The flooded images were then taken before the dams were removed in preparation for the runs. Image capture of the channel in a flooded state was recorded using identical acquisition settings, between image capture of a metric coordinate calibration plate (examples not presented in this paper) and image capture of the flow cases.

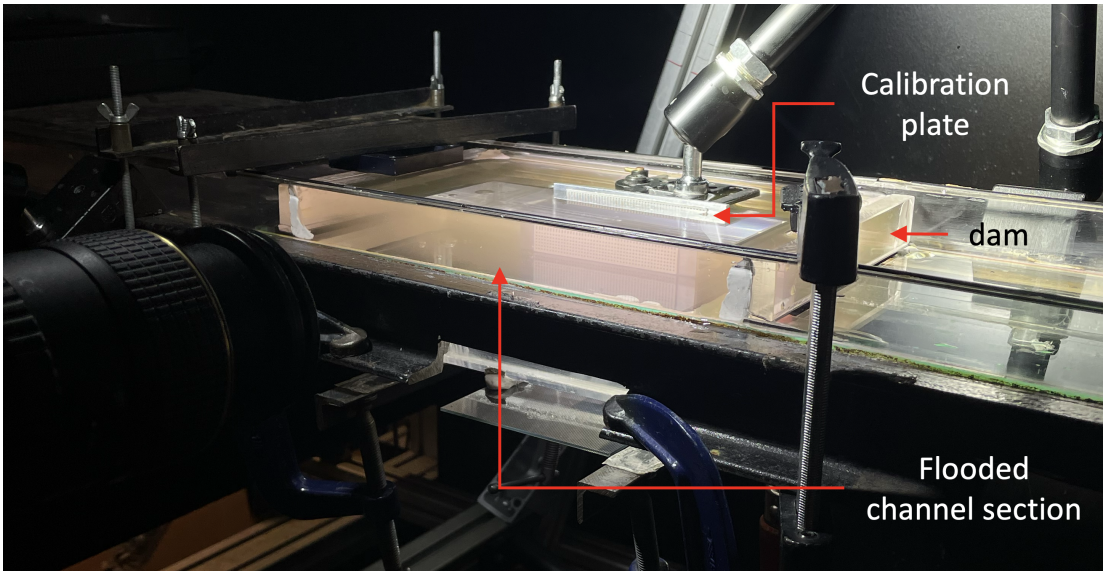

Figure 7. Channel flooded section created by temporary dams

As a part of the pre-processing, both the flooded channel image and the sample images had a two-pass median filter applied to them. As mentioned, the effect of this filtering can be seen in Figure 6 (2) and (3). The size of the median filter's first stage was 7 x 7 pixels and the second: 5 x 5 pixels. This step was integral for the removal of seeding from the images; without this, the higher intensity of light emitted by the particles generated erroneous correlation between the images (i.e. interface detection away from the actual interface).

After the application of the median filter the in-house MATLAB code then continued to analyse the now pre-processed images as follows: a digital image correlation (DIC) algorithm, custom built around MATLAB's "xcorr2", was used to cross-correlate between the flooded channel image and the sample images. A correlation window of 30 pixels wide by 1 pixel high was used, with 50 percent overlap; this was found to give the most accurate detection for the relative light column size used in this campaign; where the bright and dark regions were 10 - 15 pixels wide (after the median filter application). The correlation script scanned pixels around the interface, with the

window "moving" from bottom to top and left to right. At the point where the similarity (based on image contrast) skewed from zero, by a user defined threshold (i.e. a dissimilarity is computed), a y-coordinate was recorded, for a given x-coordinate. This was executed for every x-coordinate inside a given window.

Images (4), (5) and (6) of Fig. 6 show examples of the S-PLIF derived interface detection (green solid line) for three gas-sheared liquid film regimes, namely the stratified smooth regime (4), the 3D wave regime (5) and the disturbance/roll wave regime (6). With increase in gas shear velocity, the liquid surface becomes more rough and the amount of erroneous light scatter from the liquid film on the free surface decreases. For instance, in Image (6), only the roll wave section was affected by reflections on the free surface when compared to the base film section, where the light columns remained linear throughout. Each of these images includes a red, dashed, line that delineates where the PLIF method, which relies solely on detection based on bright/liquid to background contrast, would erroneously place the interface. A parallel submission in this conference compares film height data derived during the investigation presented in this paper to film height data obtained on the same rig using the BBLIF method (Abou Sherif et al. (2024)).

3.2. S2P-PIV image processing

In their studies, Charogiannis et al. (2019) and Voulgaropoulos et al. (2021) both used a Ronchi ruling plate and optical arrangement that utilised thin and regular rulings; 5 lines/mm and 10 lines/mm respectively. While this method would facilitate improved detection resolution, as a result of the more regular rulings, for the present campaign, a decision was made that thicker rulings of structured light be used (1 line/mm). The rationale for this is that it created for more light scatter from the bright regions of the image into the dark areas and an overall smaller attenuation of the laser light. This led to improved illumination of the seeding particles used for the PIV work. Future work on this project may include examining the effects of various ruling sizes on the detection with seeding present.

Figure 8 shows an example of how the S-PLIF detected interface coordinates were used to accurately mask both the air and liquid side images for use in simultaneous PIV. As mentioned, this process was possible since the S-PLIF and PIV processing work used the same image sets.

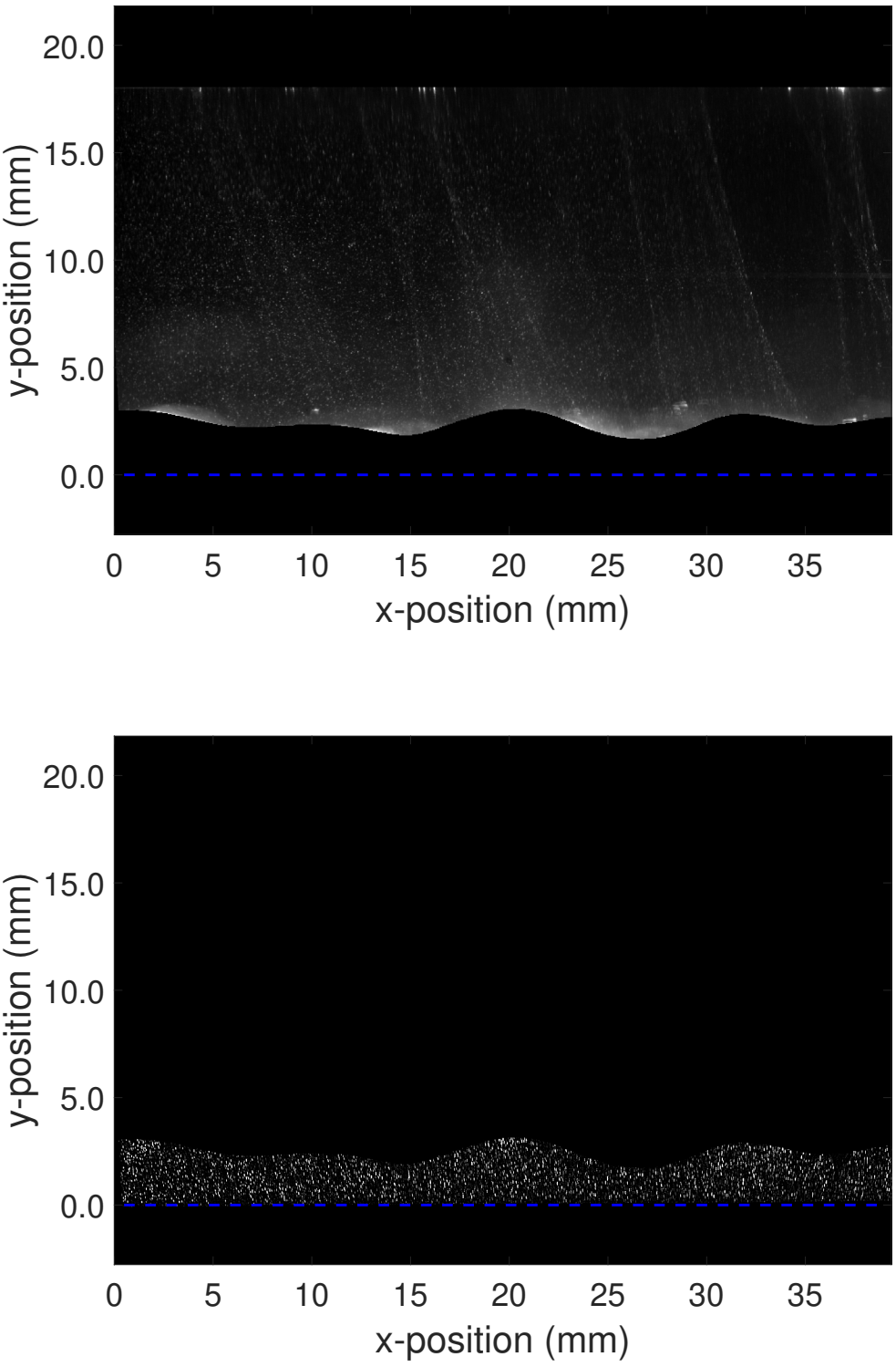

Figure 8. S-PLIF detected gas-liquid interface coordinates used for generating PIV masks; (top) air-side masked sample frame (bottom) liquid-side masked sample frame

Figure 8 shows a pair of sample masks, that were generated in MATLAB, superimposed on their

corresponding, separate, air and liquid PIV frames. The script that was used, generated two sets of unique masks for every frame of each gas and liquid data set. All masks were then imported into Dynamic Studio where the native "Dewarp" function was used to undistort and remap both the masks and raw PIV frames to a common metric coordinate system, according to a pair of dot pattern calibration images. A custom filter was applied to the liquid side images to remove the columns of light and boost the background to particle contrast. The outcome of this can be seen on the right hand image of Figure 8.

These pre-processed and dewarped image sets of the type shown in Figure 8 were then separately analysed using Dynamic Studio's Adaptive PIV algorithm to generate time-resolved velocity vector maps for each phase, with a maximum interrogation window of 64-by-64 pixels. Dantec's Adaptive PIV (Dantec Dynamics (2024)) was able to iteratively resize and reshape the interrogation area to maximise PIV cross-correlation performance, based on a predefined user preset for a minimum number of particles in a given interrogation area. This was found to be between 4 to 10 particles as per recommendations in literature Adrian (1991), Raffel et al. (2018) and Westerweel (1997).

The air-side images employed double exposure frames, where the time between pulses was set depending on superficial gas velocity (U_{SG}). The pulse duration was set to $50\ \mu s$ for the lower speeds and $20\ \mu s$ for the higher gas speeds; the presented flow case had a $30\ \mu s$ delay between pulses, for $U_{SG} = 6\ ms^{-1}$. Due to the generally slower liquid flow, the global sampling rate was tuned to to allow for adequate particle translation, in the liquid phase, between single frame images, therefore, the liquid-phase image pairs used the global sampling rate for separation time. This varied between $500\ Hz$ ($2000\ \mu s$) and $1500\ Hz$ ($666.67\ \mu s$); the presented flow case was set at $1000\ Hz$ ($1000\ \mu s$).

For each test case, these time separation values were, firstly, approximated using an image setup assistant in Dynamic Studio which used Equations 1 and 2 (Dantec Dynamics (2024)) to recommend a time-separation, where the lowest out of the two values was the suggested time separation. This was based on the predicted flow velocities and setup geometry including perceived particle diameter based on field of view and characteristics of the focal setup.

$$\Delta t_{\text{ limited by in-plane velocity}} = \left(1/4 \cdot \left(\frac{\text{geometrical IA size}}{\text{in-plane velocity}}\right)\right) \tag{1}$$

$$\Delta t_{\text{ limited by out-of-plane velocity}} = \left(1/4 \cdot \left(\frac{\text{light sheet depth}}{\text{out-of-plane velocity}}\right)\right) \tag{2}$$

The approximate time separation generated by the image setup assistant was then used as a starting point. Test runs were then conducted for each case where the time separation was increased and decreased around the recommended value to further improve PIV detection. An Adaptive PIV

interrogation area with a maximum window size of 64-by-64 pixels was used for bench-marking, to assess the chosen pulse rates; the time separation that generated the least amount of erroneous vectors was chosen for that specific run. This was repeated for all gas and liquid cases.

4. Results and discussion

4.1. Film thickness results

The dewarped and remapped coordinates of the S-PLIF defined liquid masks can be directly used to gain an abundance of information about the liquid film behaviour for regime characterisation. These masks were therefore further processed to extract this meta data for classification using statistical methods. This work is presented in a parallel paper Abou Sherif et al. (2024).

Figure 9 presents a sample space-time plot for a case with liquid flowrate, $Q_L = 8\ LPM$ and the superficial gas velocity, $U_{SG} = 10\ ms^{-1}$. The y-axis denotes the temporal state and the x-axis shows the streamwise position along the channel base. The colour bar denotes the height of the film and it can be seen that for this particular case the film height varies between 0.37 mm and 6.60 mm. A vertical line through the chart at any given x-position shows the variation of film height at that location with time over the 2.5 s sampling period. The angle of the gradients of the peaks and troughs, indicated by the changing colour bar contours gives a close approximation of the speed of the waves.

This example clearly illustrates the resolution capabilities of the capture method. Prior work using BBLIF and image analysis identified that this case has both 3D wave structures and disturbance wave structures. These qualitative features are identifiable in the space-time plot by observing the regularity and height magnitude of the signatures in the plot area, as labelled.

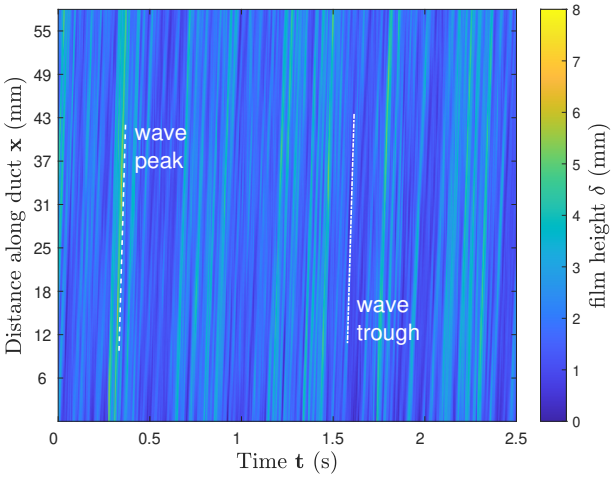

Figure 9. Sample space-time film thickness plot for case: $Q_L = 8\ LPM, U_{SG} = 10\ ms^{-1}$

This analysis approach applied to the full range of flow conditions investigated in this study is presented in Abou Sherif et al. (2024), which expands on film thickness detection features, including examination of average and statistical trends in the film thicknesses and quantitative wave characteristics. These features can be used as a platform for characterising the flow regimes and their transition boundaries. The parallel paper will also compare the effectiveness of the S-PLIF method to the BBLIF method in film thickness capture for this type of channel, as previously mentioned.

4.2. Velocity vector fields

The frame tailored masks that were created were used to separate the liquid and gas zones for PIV analysis so that simultaneous velocity data can be obtained for each phase. Figure 10 shows three sample simultaneous two-phase flow velocity vector maps, all for a liquid flow rate $Q_L = 8\ LPM$ ($U_{SL} = 0.031\ ms^{-1}$) and superficial gas velocities of $U_{SG} = 1\ ms^{-1}$ (top left) $U_{SG} = 6\ ms^{-1}$ (top right) and $U_{SG} = 10\ ms^{-1}$ (bottom). For each image the vector length is scaled to velocity with different scaling for the air (red) and liquid (blue) sections. For example, in Figure 10a) the maximum gas velocity is 3.51 m/s and the maximum liquid velocity is 0.21 m/s. For a variety of reasons it is not always possible to obtain valid velocity data for all points in the image, for example uneven light distribution can lead to insufficient illumination for some images. A velocity validation filter was used to remove erroneous data on the final output sets (this was separately applied to both phase vector maps). The velocity validation filter used a cross-correlation minimum peak height threshold followed with validation by cutting out obviously anomalous vectors. The effect of removing the erroneous vectors is that spaces with no data are present as can be seen particularly in Figure 10c).

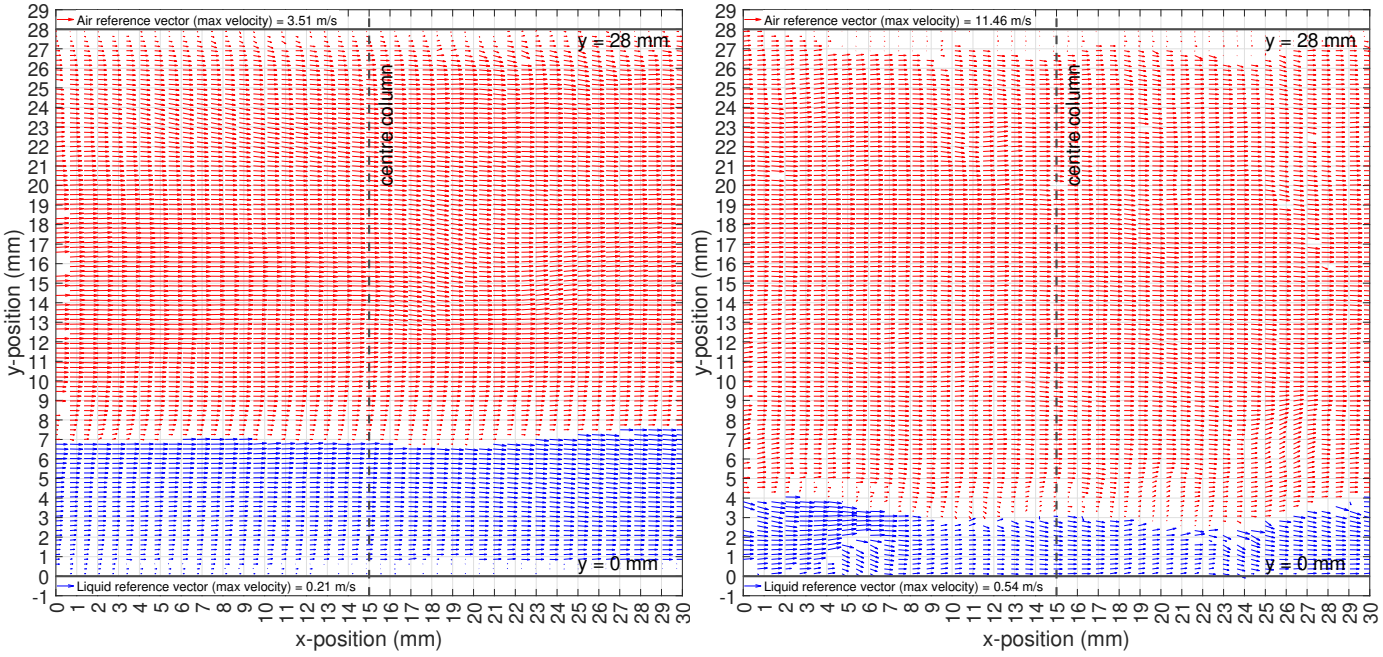

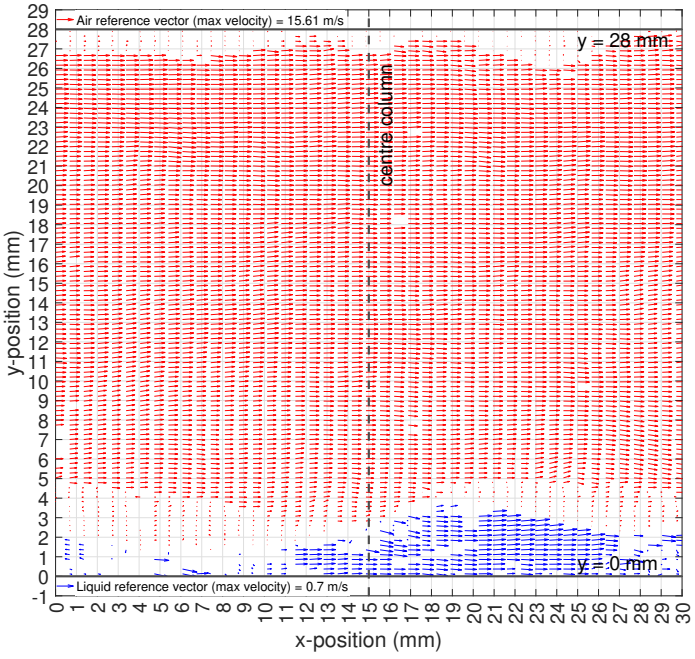

Figure 10. Sample simultaneous two-phase PIV velocity vector maps for $Q_L = 8\ LPM$ sub-cases: $U_{SG} = 1\ ms^{-1}$ (top left, a), $U_{SG} = 6\ ms^{-1}$ (top right, b) and $U_{SG} = 10\ ms^{-1}$ (bottom, c). The air-phase vectors are in red and liquid phase vectors in blue. Separate vector magnitude scaling was used for each phase (reference vector for each sub-map outlined on figure for scaling).

These vector maps present a good example of what can be achieved when using the S-PLIF method to aid in adaptive simultaneous two-phase PIV analysis. The frame tailored masking, made possible by the more accurately placed interface coordinates, facilitated discrete PIV analysis of the phases while being unaffected by each of their respective seeding. Previous PIV work conducted on this rig (Kim et al. (2018)) depended on the interface being detected from the air-side images. While equally successful, this technique had some shortcomings, most notably, a heavily reduced parametric testing range, with a maximum viable superficial gas velocity of $U_{SG} \approx 5\ ms^{-1}$ (i.e. within the 2D to 3D flow regime transition), for the present rig's geometry. This is because at higher gas velocities the gas liquid interface was sometimes not properly visible to the air-side camera. This because of the nature of the flows in regimes exhibited at higher gas shear speeds, where for example in the 3D regime, peaks in the plane closer to the camera, would block light from the interface in the zone where the light sheet is. This leads to inconsistent interface detection and sometimes cases where the interface was not detected at all. The introduction of S-PLIF interface detection has allowed for a far wider (almost unbounded within the ranges of project interest) testing scope. The current test program's parametric range has liquid flow rates in the range $1\ LPM \leq Q_L \leq 8\ LPM$ and superficial gas velocities $1\ ms^{-1} \leq U_{SG} \leq 22\ ms^{-1}$, with excellent spatial and temporal film profile detection throughout. Other limitations occur above the range of $U_{SG} \approx 14\ ms^{-1}$ as a result of increased liquid entrainment into the air phase; it was found that when transitioning into this regime instances where of the air side seeding could not be seen

occurred in some areas of the image.

While the cross-correlation from the liquid side images facilitated excellent interface detection, even in the disturbance regime, there are some other practical limitations that arose in this regime that reduced the effectiveness of the PIV cross correlation in the air, particularly at the interface (Image (6) of Figure 6 shows an image from the disturbance/roll wave regime with a roll wave highlighted for reference). When roll waves were present, their high energy nature caused the interface to become covered or unclear (on the air side images), as a result of waves, in a streamwise plane being, again, closer to the camera than the light sheet. This blocked the light scatter off the particles at the true interface. This phenomenon can be seen in Figure 11 where the arrows highlight regions where the wave troughs and corresponding interface cannot be seen because of liquid in the air between the camera and the lightsheet.

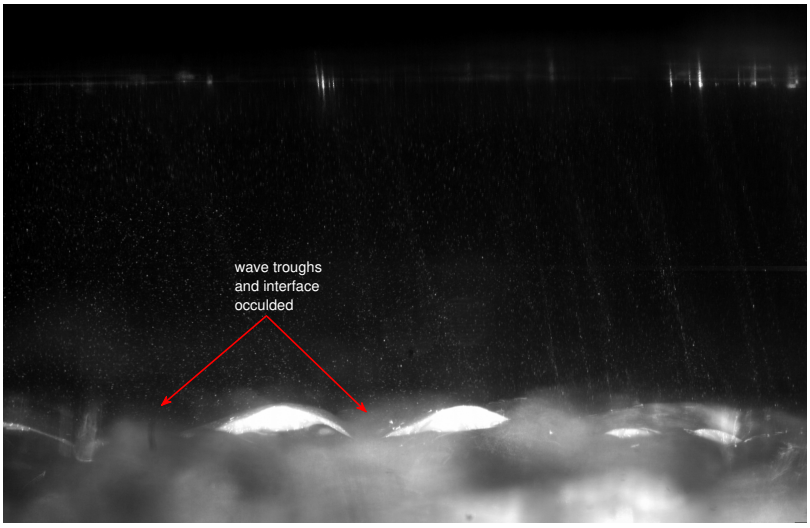

Figure 11. Air side interface occlusion due to out of plane waves on case: $Q_L = 8\ LPM\ |\ U_{SG} = 10\ ms^{-1}$

A possible solution to this issue would be to use a second laser of a different wavelength. The air seeding could then be doped with a dye that, when excited by the second laser, emits light of a different wavelength to that of the liquid side dye and a camera with the corresponding low pass filter could be used to capture only the light scatter from the dyed air seeding. While this might not eliminate the problem completely, this approach would greatly reduce the described, and other, effects of the the liquid phase light scatter (from the interface) onto the air side seeding.

4.3. First and second order velocity field analysis

Velocity data was obtained for each image for every investigated case in the parameter range of interest, namely liquid flowrates in the range 1 to 8 LPM and shearing air flowrates in the range

1 to 14 ms^{-1}. This enables statistical analysis of the flow behaviour and Figure 12a) shows two examples of extracted velocity profile data in the liquid and in the gas along the central data column for each image (ie 15 mm from the left hand edge of the image). In both cases the liquid flow rate is 8 LPM and the blue data points are for a superficial gas velocity of 2 ms^{-1} with the orange points for a superficial gas velocity of 6 ms^{-1}. Hollow markers are used for the air flow and filled markers for the liquid flow The x-axis is the axial (u) component of velocity and the y-axis gives the height location normalised to full channel height. A log scale was used on the x-axis of these plots to account for the large difference in scales between the gas phase and liquid phase velocities. An interesting feature of these plots is that the liquid velocity profile does not join to the gas velocity profile. This is because each data point is a temporal mean of an oscillating value and in the interface region the fluid present is sometimes air and sometimes liquid; the overlap is simply a feature of the wave peaks, on the liquid surface, entering and exiting the averaging domain as time elapses. Consequently there is an overlap between the gas and liquid average scatters around the interface, these regions are indicated by the boxes marked "*" on Figure 12a).

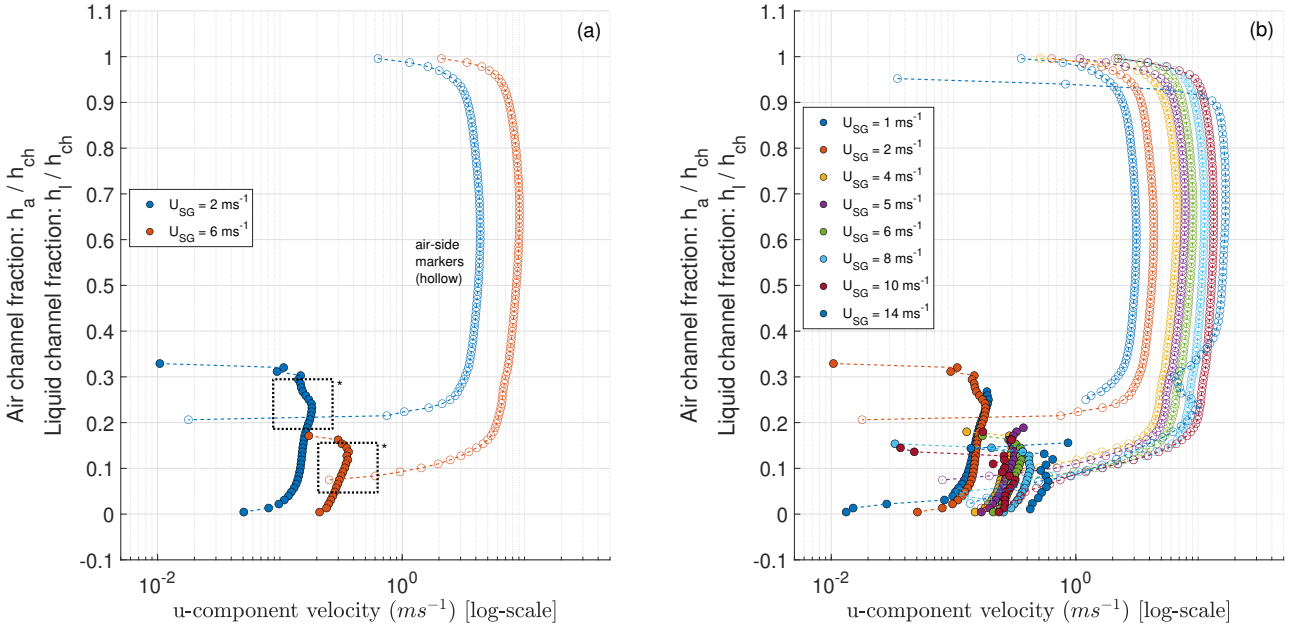

Figure 12. Temporal avg of u-component velocities of both phases along the centre column for flow case: $Q_L = 8\ LPM$; (a) shows a reduced U_{SG} data range for clarity and (b) shows full U_{SG} data range

Figure 12b) shows the temporal average axial velocity, along the centre column for a range of superficial gas velocities and a single liquid flowrate of $Q_L = 8\ LPM$. As expected, with increase in superficial gas velocity the film becomes thinner and faster, as a result of there being more energy transferred from the gas phase into the liquid phase. At $U_{SG} = 10\ ms^{-1}$ however, there was a slight decrease in mean velocity compared with that of $U_{SG} = 8\ ms^{-1}$, before the trend in liquid velocity increase was restored again at $U_{SG} = 14\ ms^{-1}$. When Cherdantsev (2023) analysed BBLIF data

from this rig they found that disturbance wave features started to appear at this velocity range, indicating that between $U_{SG} = 9\ ms^{-1}$ and $10\ ms^{-1}$ was the transition into the disturbance regime. It can be hypothesised that the short-lived decrease in mean liquid velocity at $U_{SG} = 10\ ms^{-1}$ is a result of energy transfer from the gas "propelling" the film into the disturbance regime.

The air velocity profiles of Figure 12b) all show the same general features with a boundary layer at the top, stationary channel wall, and another in the air near the film interface. The air velocity is relatively constant across much of the channel. The only velocity profile that deviates from the standard behaviour is the one for $U_{SG} = 14\ ms^{-1}$ where a local decrease in the gas phase mean velocity can be seen at around $h/h_{ch} = 0.3$. This case illustrates an effect of some of the secondary limitations that arise in the air PIV, as a result of the current configuration, when it comes to resolving high energy roll/disturbance waves as introduced in Sub-section 4.2. Previous research on this rig revealed that $U_{SG} = 14\ ms^{-1}$ is the flow case (for all liquid flow rates), where liquid entrainment occurs, from the roll section of the wave into the air. Near this roll wave peak-gas interface is where this phenomenon causes interference between the light sheet plane and the camera; here, liquid droplets being stripped from the film but present near its surface caused issues with correct particle detection in this area. Furthermore, increased reflections occur near the gas-wall interface, as a result of the liquid misting into the air. The effects of this can be seen by the slight discontinuity in velocity data in this area, around $h/h_{ch} = 1$, where the stationary air-wall boundary became less visible. Further analysis is planned to asses these phenomena more closely.

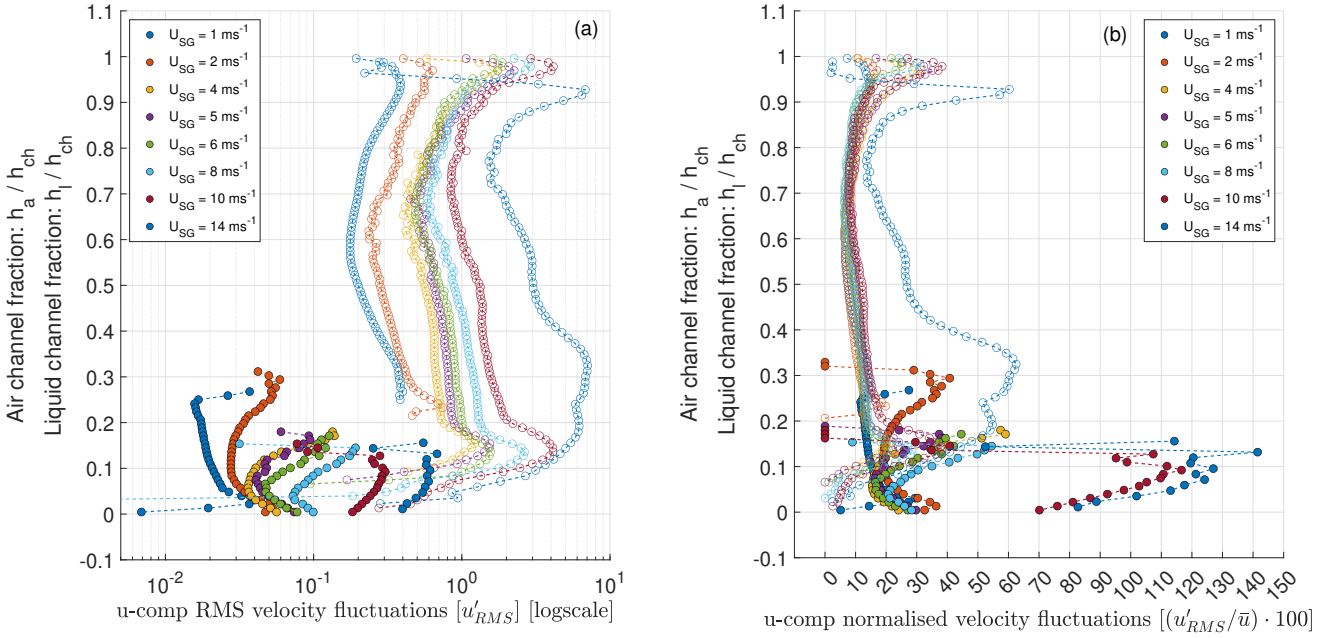

Figure 13. Temporal avg of u-component (a): RMS velocity fluctuations (u'_{RMS}) and (b): mean normalised velocity fluctuations ($u'_{RMS}/\bar{u}$) of both phases along the centre column for flow case: $Q_L = 8\ LPM$

Figure 13a) shows the root-mean-square (RMS) values of axial velocity fluctuations (u'_{RMS}) while Figure 13b) shows the velocity fluctuations normalised by the mean velocity (for the liquid or the gas, different for each phase) ($u'_{RMS}/\bar{u}$). In both graphs the y-axis is the normalised channel height. Figure 13a) illustrates that the velocity fluctuation is far lower in the liquid compared to the gas but when normalised to the mean velocity (Figure 13b) it can be seen that for most liquid flow rates comparable values to the gas are obtained but with far higher values for the higher shearing air flow velocities.

A feature of interest in the data on Figure 13a) is the change in the liquid phase velocity fluctation behaviour beyond $U_{SG} = 8\ ms^{-1}$. The graph shows that all the liquid u'_{RMS} curves, up to $U_{SG} = 8\ ms^{-1}$, can be split into two different "sub-curves"; closer to the wall the fluctuation decreases exponentially with distance from the wall (linear on log scale), before changing to an increasing relationship after a certain distance (unique to each curve) away from the wall. The increase is close to exponential for gas velocities between 5 and 8 ms^{-1}. However, the curves of cases $U_{SG} = 10\ ms^{-1}$ and $U_{SG} = 14\ ms^{-1}$ do not have the decreasing section, exhibiting almost a single relationship throughout. This change in behaviour further supports the idea that there is a regime transition region that starts between $U_{SG} = 9\ ms^{-1}$ and $U_{SG} = 10\ ms^{-1}$.

On the plot for normalised velocity fluctuations (Figure 13b), it can be seen that the curves for $U_{SG} = 10\ ms^{-1}$ and $U_{SG} = 14\ ms^{-1}$ exhibit different behaviour compared to the remainder of the curves. Furthermore, normalised velocity fluctuation for these cases can be described as abnormally high; reaching in excess of 130%. Since ($u'_{RMS}/\bar{u}$) is a statistically driven number, planned future analysis will investigate the statistical analysis of the velocity distributions to better characterise the flow regimes from phase velocity distribution trends such as curve skewness and position of the medians.

4.4. Applications note

This experimental work has a great deal of applicability for the validation of relevant CFD co-current two-phase flows. The results of these experiments were used, so far, to generate film thickness data for a large number of flow cases (more details presented in the parallel paper: Abou Sherif et al. (2024)) as well as phase velocity data, in this paper. Further to this, the work has been used to characterise the different regimes, which are often not naturally approximated by CFD models, allowing for closer turbulence and interface dynamics considerations when modelling.

One example is in the work of Bertolotti et al. (2022), which researched the inability of Reynolds-Averaged Navier-Stokes (RANS) models to predict appropriate interfacial turbulence levels in flows similar to the ones researched in the present experimental work. It was found that the commonly used standard $k-\omega$ turbulence model, led to inaccuracies in the prediction of the film thick-

ness as a result of turbulence level over-prediction at the interface. Bertolotti et al. (2022)'s research later made use of experimental data from Fabre et al. (1987) to validate quasi direct numerical simulation (quasi-DNS) of the available thick film cases. This work then went on to generate a modified RANS $k-\omega$ model by adding a correction source term from the high fidelity quasi-DNS work.

The limited number of cases conducted in the experimental research of Fabre et al. (1987) meant that only thick films in the stratified smooth regime could be analysed in CFD. The current research, which improves on two-phase flow PIV capture as a result of using S-PLIF for interface detection, has increased the parametric range greatly up to the disturbance regime where $U_{SG} \geq 10\, ms^{-1}$.

5. Summary and conclusions

The work included in this paper shows the effectiveness of using the S-PLIF method to facilitate more accurate analysis of simultaneous two-phase gas-liquid stratified PIV captured using only two cameras by providing a repeatable and accurate method of identifying the interface location. The S-PLIF data-sets have enabled the generation of accurate masks for the individual phases thereby enabling application of PIV cross-correlation algorithms in the appropriate individual phase regions despite both being seeded with particles. The more accurate interface coordinates have not only aided in improving PIV accuracy, but have allowed for a larger parametric range to be examined by nature of the clearer identification of the extent of the liquid phase from the S-PLIF images when, compared to the prior approach that employed interface detection from the air-side images.

Processing limitations that affected air-side data in the higher energy cases, starting at $U_{SG} = 10\ ms^{-1}$, were discussed in this paper. These limitations arose as a consequence of the higher energy nature of interface regimes in these flow cases (disturbance/roll waves). It was found that roll waves often caused misting near the interface and this, coupled with spanwise out-of-plane waves, often created occlusion between the light sheet plane and the camera.

First and second order statistical analysis of axial velocity for each phase was also presented in this paper illustrating how flow regimes could be identified by observing changes in the various curve trends on the plots for temporal average (along the centre column) of phase velocities, RMS of velocity fluctuations and the normalised velocity fluctuations. The mean values and curve profiles of cases $U_{SG} = 10\ ms^{-1}$ and $U_{SG} = 14\ ms^{-1}$ were different to those of the lower U_{SG} cases and this is attributed to these two cases being in the disturbance/roll wave regime.

The applications of the work to CFD model development were also discussed in this paper; a good example of where this data is applicable is in the expansion of quasi-DNS informed RANS

models in areas where turbulence is often incorrectly predicted when using standard averaged CFD models, such as near the interface. The increased parametric range tested in the present experimental campaign introduced opportunity to validate and inform CFD models in regimes beyond smooth interfaces in the relevant stratified co-current two-phase flows.

Acknowledgements

The authors would like to thank Rolls Royce plc and the EPSRC for their support under the Prosperity Partnership Grant Cornerstone Mechanical Engineering Science to Enable Aero Propulsion Futures, Grant Ref: EP/R004951/1.

The authors would also like to thank Ivan Zadrazil of Dantec Dynamics for his comprehensive support and advice during the S-PLIF and PIV analysis stage.

References

Abou Sherif, A., Johnson, K., & Hann, D. B. (2023). Investigation of the effects of fluid velocity and liquid properties on the multiphase regimes in horizontal rectangular ducts. In *11th international conference on multiphase flow.* Kobe.

Abou Sherif, A., Johnson, K., & Hann, D. B. (2024). Comparative Analysis of Brightness-Based Laser-Induced Fluorescence (BBLIF) and Structured Planar Laser-Induced Fluorescence (S- PLIF) for Film Thickness Measurement in Two-Phase Flow. In *21st international symposium on applications of laser and imaging techniques to fluid mechanics.* Lisbon.

Adrian, R. (1991). Particle-Imaging Techniques For Experimental Fluid-Mechanics. *Annual Review of Fluid Mechanics*. doi: 10.1146/annurev.fluid.23.1.261

Bertolotti, L., Richard, J.-L., & Ambrose, S. (2022). *Machine Learning-Augmented Turbulence Models for the Simulation of Two-Phase Shearing Flows* (Unpublished doctoral dissertation).

Charogiannis, A., Denner, F., van Wachem, B. G., Kaliadasis, S., & Markides, C. N. (2018). A combined experimental and computational study of the heat transfer characteristics of falling liquid-films. In *Proceedings of the thermal and fluids engineering summer conference* (Vol. 2018-March, pp. 985–994). doi: 10.1615/TFEC2018.fmp.021505

Charogiannis, A., & Markides, C. N. (2019, 10). Spatiotemporally resolved heat transfer measurements in falling liquid-films by simultaneous application of planar laser-induced fluorescence (PLIF), particle tracking velocimetry (PTV) and infrared (IR) thermography. *Experimental Thermal and Fluid Science*, *107*, 169–191. doi: 10.1016/j.expthermflusci.2018.11.001

Charogiannis, A., Sik An, J., Voulgaropoulos, V., & Markides, C. N. (2019, 9). Structured planar laser-induced fluorescence (S-PLIF) for the accurate identification of interfaces in multiphase flows. *International Journal of Multiphase Flow*, *118*, 193–204. doi: 10.1016/j.ijmultiphaseflow.2019.06.002

Cherdantsev, A. V. (2023, 7). Three-dimensional evolution and interaction of disturbance waves on a gas-sheared liquid film on a horizontal plane near the transition region. *International Journal of Multiphase Flow*, *164*, 104468. doi: 10.1016/J.IJMULTIPHASEFLOW.2023.104468

Cherdantsev, A. V., Hann, D. B., & Azzopardi, B. J. (2014, 12). Study of gas-sheared liquid film in horizontal rectangular duct using high-speed LIF technique: Three-dimensional wavy structure and its relation to liquid entrainment. *International Journal of Multiphase Flow*, *67*, 52–64. doi: 10.1016/j.ijmultiphaseflow.2014.08.003

Cherdantsev, A. V., Sik An, J., Charogiannis, A., & Markides, C. N. (2018). Cross-Validation of PLIF and BBLIF towards the Detailed Study of Gas-Sheared Liquid Films in Downward Annular Flows. In *19th international symposium on the application of laser and imaging techniques to fluid mechanics.* Retrieved from `https://www.researchgate.net/publication/327141267`

Cherdantsev, A. V., Sik An, J., Charogiannis, A., & Markides, C. N. (2019, 10). Simultaneous application of two laser-induced fluorescence approaches for film thickness measurements in annular gas-liquid flows. *International Journal of Multiphase Flow*, *119*, 237–258. doi: 10.1016/j.ijmultiphaseflow.2019.07.013

Dantec Dynamics. (2024). *DynamicStudio User's Guide Version 8*. Dantec Dynamics.

Fabre, J., Suzanne, C., & Masbernat, L. (1987). Experimental data set no. 7: stratified flow, part i: Local structure. *Multiphase Science and Technology*, *3*(1-4), 285–301. Retrieved from `http://www.dl.begellhouse.com/journals/5af8c23d50e0a883,6b4442405c7a2bae,23ace2da6ef09e09.html` doi: 10.1615/MultScienTechn.v3.i1-4.120

Hann, D. B., Cherdantsev, A. V., & Azzopardi, B. J. (2018, 11). Study of bubbles entrapped into a gas-sheared liquid film. *International Journal of Multiphase Flow*, *108*, 181–201. doi: 10.1016/j.ijmultiphaseflow.2018.07.001

Kim, J.-H., Hann, D., & Johnson, K. (2018). *Time-resolved simultaneous PIV measurements of an air-shear-driven thin film flows in a rectangular duct* (Tech. Rep.). Mechanical and Aerospace Systems Research Group (formerly Gas Turbine and Transmissions Research Centre), University of Nottingham.

Raffel, M., Willert, C. E., Scarano, F., Kähler, C. J., Wereley, S. T., & Kompenhans, J. (2018). *Particle Image Velocimetry A Practical Guide* (3rd ed.). Springer. Retrieved from `https://link-springer-com.nottingham.idm.oclc.org/book/10.1007/978-3-319-68852-7`

Sinha, A., Cherdantsev, A., Johnson, K., Vasques, J., & Hann, D. (2021, 12). How do the liquid properties affect the entrapment of bubbles in gas sheared liquid flows? *International Journal of Heat and Fluid Flow*, *92*. doi: 10.1016/j.ijheatfluidflow.2021.108878

Voulgaropoulos, V., Patapas, A., Lecompte, S., Charogiannis, A., Matar, O. K., De Paepe, M., & Markides, C. N. (2021, 9). Simultaneous laser-induced fluorescence and capacitance probe measurement of downwards annular gas-liquid flows. *International Journal of Multiphase Flow*, *142*. doi: 10.1016/j.ijmultiphaseflow.2021.103665

Westerweel, J. (1997). Fundamentals of digital particle image velocimetry. *Measurement Science and Technology*, *8*.